Radiocarbon Variability in the Western North Atlantic During the Last Deglaciation

Laura F. Robinson,[1]* Jess F. Adkins,[1] Lloyd D. Keigwin,[2] John Southon,[3] Diego P. Fernandez,[1] S-L Wang,[1] Daniel S. Scheirer[4]

We present a detailed history of glacial to Holocene radiocarbon in the deep western North Atlantic from deep-sea corals and paired benthic-planktonic foraminifera. The deglaciation is marked by switches between radiocarbon-enriched and -depleted waters, leading to large radiocarbon gradients in the water column. These changes played an important role in modulating atmospheric radiocarbon. The deep-ocean record supports the notion of a bipolar seesaw with increased Northern-source deep-water formation linked to Northern Hemisphere warming and the reverse. In contrast, the more frequent radiocarbon variations in the intermediate/deep ocean are associated with roughly synchronous changes at the poles.

The last deglaciation was punctuated by numerous distinct millennial-scale climate events (*1*, *2*), and understanding the mechanisms behind these changes is a major goal of paleoceanography. The deep ocean stores and transports heat and carbon, so changes in its circulation are likely to influence global climate. Indeed, alternating the main site of deep-water formation between the Northern and Southern hemispheres has been linked to switches in the amount of cross-equatorial heat transport (*3*). This bipolar seesaw predicts sizable changes in mass transport in the deep North Atlantic and may be the cause of anti-phase warm and cool periods observed in Greenland and Antarctic ice cores during the last deglaciation (*1*, *2*) (Fig. 1). Well-dated high-resolution records are needed to make a mechanistic connection between deep-ocean circulation and climate. Passive geochemical tracers from marine sediments show us that during the last glacial maximum (LGM), Northern-source water (NSW) overlay Southern-source water (SSW), with the boundary at ~2,000 m in the western North Atlantic (*4*, *5*). The transition from the LGM to the modern state, where North Atlantic Deep Water (NADW) dominates the Western basin, was marked by a series of changes in the deep-ocean circulation pattern (*6*, *7*). To help characterize those changes more completely, we have made $^{14}C/^{12}C$ measurements of well-dated samples of the deep-sea coral *Desmophyllum dianthus* (*8*).

A radiocarbon age can be deduced for a given water mass if its radiocarbon content (^{14}C 5730 year half-life) is known both when it forms and when it reaches the deep ocean. By making depth profiles of $\Delta^{14}C$ in the past (*9*), we can investigate variability in deep-ocean $\Delta^{14}C$ values and begin to put constraints on changes in ocean circulation. Deep-sea radiocarbon records can also be used to investigate the role of the ocean in modulating the atmospheric carbon reservoir. The ocean contains ~60 times as much carbon as the atmosphere, so small changes in uptake or release of radiocarbon from the ocean may cause large changes in atmospheric $\Delta^{14}C$. Today, radiocarbon-enriched NADW formation draws down atmospheric ^{14}C more efficiently than radiocarbon-depleted Antarctic Bottom Water (AABW) formation, so varying the proportion of NSW to SSW or changing the flux of NSW are both likely to change atmospheric $\Delta^{14}C$. Our record of ocean $\Delta^{14}C$ lets us constrain the influence of the deep ocean on atmospheric radiocarbon.

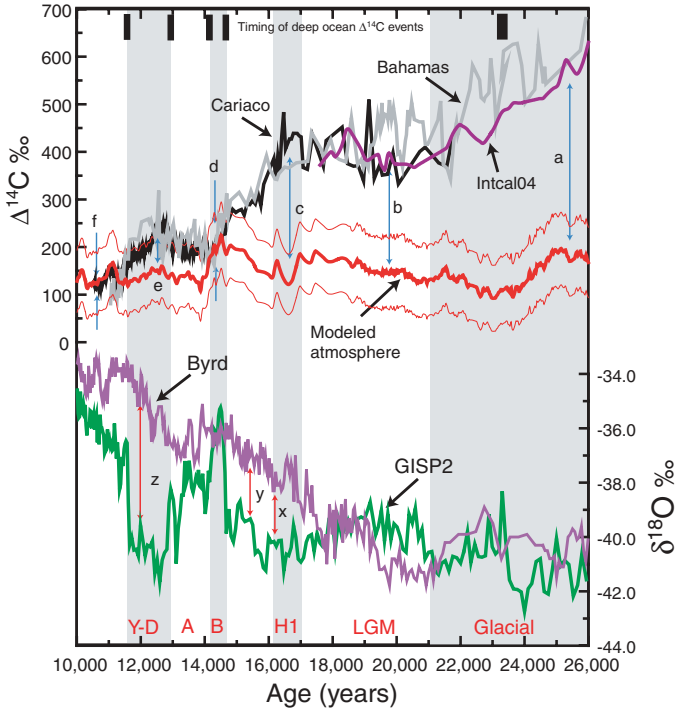

Fig. 1. The top three curves are observed atmospheric $\Delta^{14}C$ records: Cariaco Basin in black (*34*), a Bahamas speleothem in gray (*35*), and Intcal04 in purple (*39*), which, during the main period of interest, is primarily based on precisely dated surface coral data (*53*). All of these records are in reasonable agreement from 10 ka back to ~15.5 ka, but there are differences during Heinrich 1. The age model for the Cariaco Basin is poorly constrained during Heinrich 1, with the exception of a distinct change in gray-scale that matches a $\delta^{18}O$ event in both GISP2 and a U-Th dated speleothem from Hulu Cave (*54*) at 16.0 ka. Two outliers have been removed from the Cariaco record (16.10 ka and 17.96 ka). Between 26 and 22 ka, we plot only the Intcal04 (*39*) and speleothem data (*35*), which are consistent with one another. When comparing our ocean $\Delta^{14}C$ data to the atmosphere, we refer to Intcal04 (*39*) except between 17.5 ka and 14.5 ka, where there are no surface coral data and the record is poorly constrained. In this 3000-year period, we combine the Cariaco (*34*) and speleothem records (*35*) as our best estimate of the atmosphere. The ^{10}Be-based $\Delta^{14}C$ (modeled) reconstruction is plotted on the same scale as the observed atmospheric record, with the maximum and minimum as thin lines and the mean as a thick red line (*36*). Arrows a to f and x to z point to times that are referred to in the text. The GISP2 (green) and Byrd $\delta^{18}O$ (purple) records are plotted after Blunier and Brook (*2*).

[1]California Institute of Technology, MS 100-23, 1200 East California Boulevard, Pasadena, CA 91125, USA. [2]McLean Lab, Department of Geology and Geophysics, Woods Hole Oceanographic Institution, Woods Hole, MA 02543, USA. [3]Earth System Science Department, 3200 Croul Hall, University of California, Irvine, CA 92697–3100, USA. [4]U.S. Geological Survey, 345 Middlefield Road, MS989, Menlo Park, CA 94025, USA.

*To whom correspondence should be addressed. E-mail: laurar@gps.caltech.edu

Using radiocarbon as a circulation tracer has been successful in the modern ocean. NADW and AABW have end-member values of –65‰ (per mil) and –165‰, respectively (*10*, *11*). Radioactive decay causes deviations below the mixing line of these two end members, allowing us to calculate the radiocarbon age of the water in the North Atlantic (*12*). In the modern western North Atlantic [GEOSECS (Geochemical Ocean Section Study) Station 120, 33°16′N], the water column has a small vertical $\Delta^{14}C$ gradient (~10‰ /1000 m) consistent with a single northern-source water mass (*13*). By contrast, farther south in the Atlantic, NADW is underlain by southern-sourced AABW. AABW has a characteristic low $\Delta^{14}C$ because the "old" Pacific intermediate water from which it forms is not at the surface long enough to reequilibrate with the atmosphere. In the past, this approach is complicated by variability in the two end-member $\Delta^{14}C$ values at the sites of deep-water formation (*14*). For example, increasing the extent of sea-ice cover would allow less air-sea gas exchange and, therefore, less radiocarbon in AABW. Constraints on the past deep-ocean $\Delta^{14}C$ have been acquired using the radiocarbon ages of benthic and planktonic foraminifera (BF-PF) and the aragonitic skeletons of deep-sea corals. In the foraminifera, the planktonic age can be converted to a calendar age, and the benthic $^{14}C/^{12}C$ ratio can then be used to calculate deep-ocean $\Delta^{14}C$. Early $\Delta^{14}C$ reconstructions suffered from problems of species-dependent age variability in planktonic $^{14}C/^{12}C$ measurements (*15*–*18*), but this problem is alleviated by targeting depths with high foraminiferal abundances or high sedimentation rates (*19*).

Deep-sea corals, typically found at water depths of ~500 to 2500 m, are datable by U-Th techniques and are good archives of palaeo-$\Delta^{14}C$ (*20*–*24*). Individual corals with different calendar ages can be compared with one another to give a resolution similar to that of ocean sediment cores. The solitary coral *D. dianthus* is thought to have a life span of ~100 years (*25*), so each individual skeleton can be subsampled for $^{14}C/^{12}C$ to construct decadal-resolution records of radiocarbon variability, comparable to the temporal resolution of ice-core climate records (*20*). We collected more than 3700 *D. dianthus* corals from the New England Seamounts in May 2003 (*26*). U-Th isotopic measurements were made by isotope dilution, and 27 samples were selected for $^{14}C/^{12}C$ analysis (*27*) (table S1). Nine of these corals were subsampled to produce high-resolution transects of $\Delta^{14}C$. Our second sample set consists of 12 BF-PF pairs [spanning 19.5 thousand years ago (ka) to 10.7 ka] from the western North Atlantic and one additional sample using a benthic bivalve found in the core (table S2). Combining these data with published deep-sea corals and BF-PF pairs (*19*, *20*, *28*–*32*) allows us to reconstruct a detailed history of radiocarbon from the last glacial through to the Holocene.

Discussion. The ^{14}C content of the atmosphere and the deep sea are coupled, but our knowledge of the history of these two reservoirs is vastly different. The history of radiocarbon variability in the atmosphere is reasonably well constrained through the LGM and beyond (*33*–*35*). Radiocarbon and ^{10}Be are produced in the upper atmosphere simultaneously, and because ^{10}Be is not subject to decay or uptake in the carbon cycle, it can be used as a proxy for the ^{14}C production rate alone (*36*). Muscheler *et al*. (*36*) estimate the ^{10}Be production rate from the measured ^{10}Be content of Greenland ice cores and convert it to an expected atmospheric $\Delta^{14}C$ record, assuming that the present-day carbon cycle was the same throughout (hereafter referred to as modeled atmospheric $\Delta^{14}C$) (Fig. 1) (*37*, *38*). Changes in observed atmospheric $\Delta^{14}C$ that are greater than predicted from the production rate curve alone must be due to deviations from the assumed modern steady state, implying changes in the deep-ocean uptake on this 10^3- to 10^4-year time scale (*34*–*36*).

Compared with the atmosphere, our knowledge of the deep ocean is more limited, both in depth and in time. Our data fill this knowledge gap, allowing us to compare $\Delta^{14}C$ at depth intervals in the western North Atlantic directly with the changes observed in the atmosphere (Fig. 2). A contour plot of the history of oceanic radiocarbon relative to atmospheric radiocarbon provides a true-age chronology through the glacial and deglacial periods (Fig. 3). It is clear from this plot that intermediate-deep (I/D) (1700 to 2500 m) waters are more variable than the abyss. A horizontal $\Delta^{14}C$ divide separates water masses above and below ~2,500 m, and NSW penetrates below this divide only twice during the deglaciation. A deglacial,

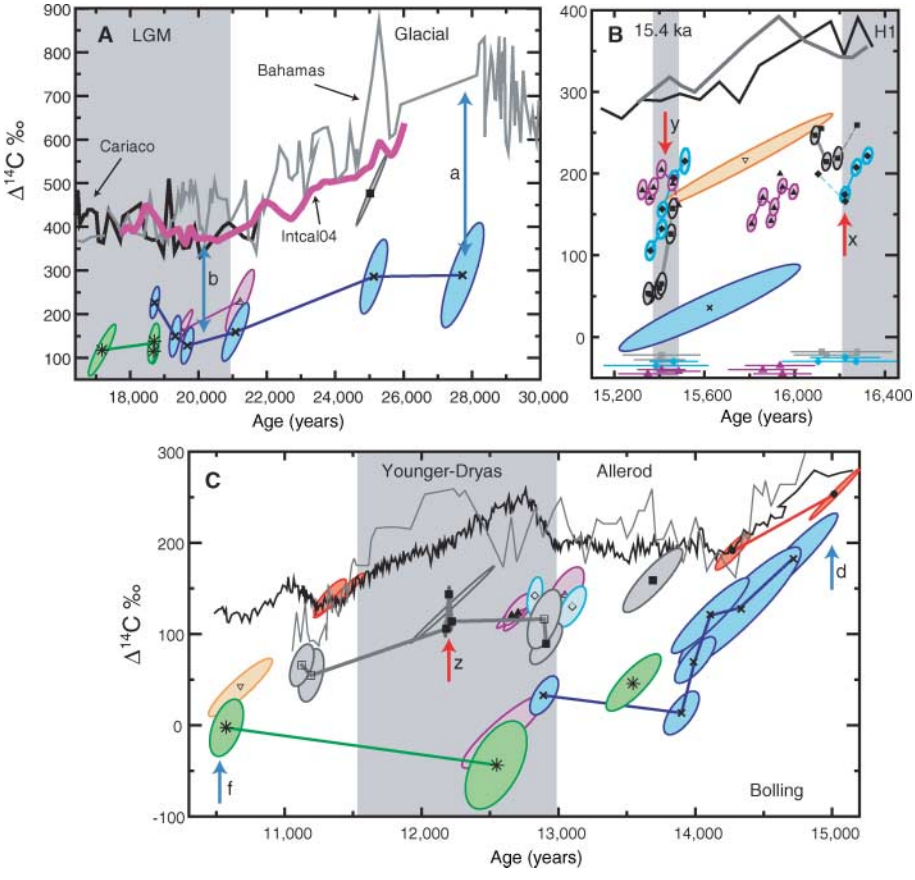

Fig. 2. Raw $\Delta^{14}C$ data for (**A**) 30.0 to 16.4 ka, (**B**) 16.4 to 15.1 ka, and (**C**) 15.1 to 10.0 ka, compartmentalized into seven depth bands: 1176 to 1221 m (red circles), 1381 to 1400 m (orange upside-down triangles), 1713 to 1790 m (black squares), 1886 to 2155 m (pale blue diamonds), 2228 to 2590 m (purple triangles), 2972 to 3845 m (blue crosses), and 4055 to 4712 m (green stars) below sea level. Each record is plotted against calendar age before the present (B.P.), with 2-SE error ellipses. Open symbols, crosses, and stars are BF-PF pairs; closed symbols are corals. One published Younger Dryas BF-PF data point (*19*) is not plotted because it lies above the atmospheric curve. In Fig. 2B, color-coded 2-SE calendar-age error bars are shown as horizontal bars, with error ellipses representing the relative error between individual points on the same coral. Solid lines join $\Delta^{14}C$ measurements from within one coral; dashed lines connect data from separate corals. Two coral data points (1886 m, 16.1 ka and 2500 m, 15.9 ka) are not shown because they have large calendar-age errors that overlap other data points (242 and 297 years, respectively). The two points with large error ellipses that are shown are BF-PF pairs.

radiocarbon-depleted I/D water mass (akin to modern Antarctic Intermediate Water) is present at 40°N during Heinrich 1, the 15.4-ka event, and the Younger Dryas.

Glacial Ocean. From 28 to 17 ka, the $\Delta^{14}C$ of the western North Atlantic is constrained by 12 points (11 BF-PF pairs and 1 coral) (Fig. 2A). The 25-ka coral at 1700 m has a $\Delta^{14}C$ only 66‰ lower than the atmosphere, indicative of well-ventilated NSW. By contrast, all deeper samples are more depleted in radiocarbon than anywhere in the modern ocean. This depletion is >400‰ at 28 ka and drops to ~230‰ during the LGM (Fig. 2A, arrows a and b, and Fig. 4A). A slowdown in the ventilation rate or a change in the proportion of NSW to SSW may account for some of this observed $\Delta^{14}C$ shift in the deep ocean. However, Cd/Ca ratios show us that the LGM deep North Atlantic was filled by SSW (*6*), and the pattern of deep-sea $\Delta^{14}C$ from 21 to 18.7 ka reflects the atmosphere nearly synchronously, suggesting that this SSW water was circulating vigorously (*39*) (Fig. 2A). An alternative cause of radiocarbon depletion in the Southern Ocean is extensive sea-ice coverage, which would reduce the amount of the air-sea carbon exchange. In support of this mechanism, diatom-based reconstructions show that the LGM sea-ice extent was 5° farther north than in the present day and that before the LGM, the sea ice exhibited less seasonal variability (*40–42*). Over the same time period, from 30 ka to the LGM, the observed and modeled $\Delta^{14}C$ of the atmospheric records converged from a large offset of >350‰ to ~250‰ (Fig. 1, arrows a and b). We suggest that the reduction in the atmospheric ^{14}C content was caused by an increase in the ^{14}C uptake in the Southern Ocean. Not only would such a change in the Southern Ocean affect the $\Delta^{14}C$ of North Atlantic water but, as the dominant source to the deep Pacific, it could alter the whole ocean ^{14}C inventory.

Heinrich 1 and the 15.4-ka event. Heinrich events are characterized by massive ice-rafted debris (IRD) deposits in the North Atlantic (*43*), and it has been suggested that these large freshwater inputs in the Northern Hemisphere may reduce the rate of northern-sourced deep-water formation by lowering the density of surface water. The Pa/Th ratio of a marine sediment record from 4500 m at the Bermuda Rise shifts toward values indicative of such a reduction during Heinrich 1 (*44*). As expected, this slowdown in NSW flux is consistent with a reduction in the amount of uptake of ^{14}C by the deep Atlantic and a divergence in the modeled and observed atmospheric records (Fig. 1, arrow c), although the signal is not large.

During Heinrich 1, the $\Delta^{14}C$ water-column profile is characterized by radiocarbon-rich water overlying radiocarbon-poor water (Fig. 4A), indicative of a greater proportion of SSW deeper in the water column. This deep water in the North Atlantic has the same offset from the atmosphere as the southern-source end member (~265‰, constrained by a 16.7-ka deep-sea coral from the Drake Passage) (*21*), which implies a vigorous deep SSW circulation. These radiocarbon data are not consistent with the Bermuda Rise Pa/Th record (*44*) if the latter is interpreted as a dramatic reduction of deep-water ventilation rate. On the other hand, our data show the $\Delta^{14}C$ of I/D water decreasing through Heinrich 1, consistent with a reduction in NSW flux (Fig. 2B). Six coral individuals describe a "U-shaped" change in $\Delta^{14}C$ in the I/D ocean beginning at 16.3 ka (Fig. 2B, arrow x). Multiple measurements from within one coral at 2,000 m define a $\Delta^{14}C$ decrease of 50‰ in ~100 years (Fig. 2B). This decrease occurred faster than the rate of ^{14}C decay, so it must be due, at least in part, to mixing-in of low $\Delta^{14}C$ SSW. This downward trend reverses at 16.2 ka, when multiple ^{14}C measurements within a second coral define a 30‰ rise in $\Delta^{14}C$ caused by an increase in the influence of radiocarbon-rich NSW (Fig. 2B). The timing of the turn in the $\Delta^{14}C$-U-shape, 16.2 ka, is coincident with the start of the dramatic decrease in $\Delta^{14}C$ observed in the atmosphere (within calendar-age error limits) and signals the end of Heinrich 1 at I/D depths.

After Heinrich 1, at 15.5 ka, all corals from 1700 to 2500 m have a $\Delta^{14}C$ signal ~100‰ lower than the atmosphere, indicative of a

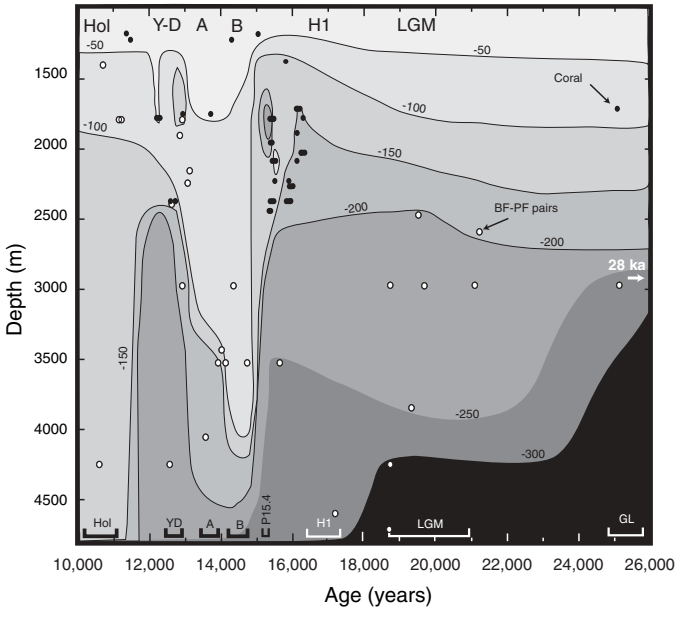

Fig. 3. Cartoon contour plot for all coral (closed circles) and BF-PF (open circles) data from 26 to 10 ka and deeper than 1000 m in the western North Atlantic. Data are plotted relative to the atmospheric record shown in Fig. 1. Dark colors are low in radiocarbon, and light colors are rich in radiocarbon. One BF-PF sample from 27.7 ka (*19*) lies off the time axis; it is from 2972 m and has a >400‰ offset from the atmosphere. Brackets at the bottom show the time intervals for the depth profiles in Fig. 4.

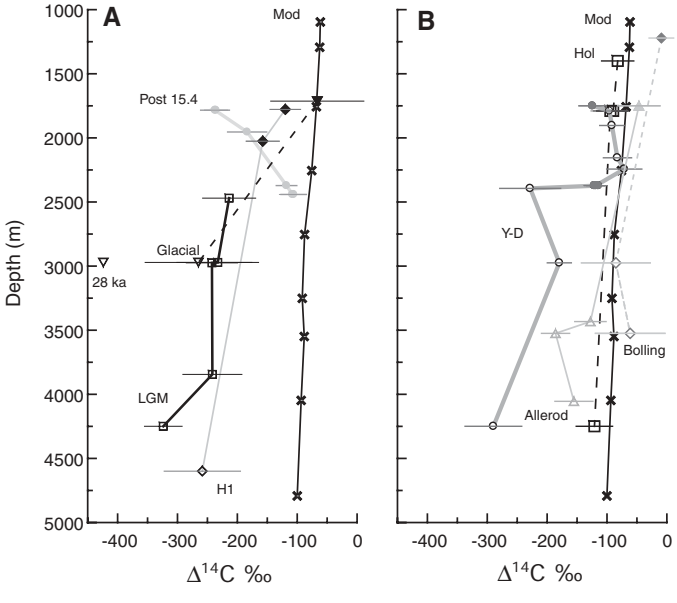

Fig. 4. Depth profiles of $\Delta^{14}C$ relative to the atmosphere in the ocean are chosen from discrete time slices (**A**) from the glacial to 15.4 ka and (**B**) from the Bolling to the Younger Dryas. Modern GEOSECS water column data are shown as crosses in both panels (*13*). Open symbols are BF-PF pairs; closed symbols are corals. The data in each profile are bracketed in Fig. 3 and marked in table S3. These profiles are not representative of "steady-state" ocean configurations, but they are plotted to demonstrate the large and variable radiocarbon gradients in the deep and I/D ocean.

well-mixed, well-ventilated northern-source I/D water column. Deeper, at 3500 m, SSW still fills the deep-water column, as shown by a BF-PF pair with a 250‰ offset from the atmosphere (Fig. 2B).

The modeled and observed atmospheric $\Delta^{14}C$ records converge after Heinrich 1. This convergence is interrupted by a plateau in the atmospheric $\Delta^{14}C$ record that lasts from ~15.7 to 15.0 ka and is coincident with a pause in the deglacial temperature rise in both hemispheres (Fig. 1, arrow y). At water depths of 1700 to 2000 m, this 15.4-ka event is characterized by a massive and rapid (100‰ in ~100 years) drop in $\Delta^{14}C$ (*20*) (Fig. 2B, arrow y). Multiple ^{14}C measurements within the lifetime of each of four individual corals from two different seamounts clearly define this trend. The decrease is much faster than in situ decay of ^{14}C and must be due to mixing-in of low $\Delta^{14}C$ SSW. A $\Delta^{14}C$ decrease is also seen at 2500 m, but with a lesser amplitude (~40‰). We interpret this change as a ^{14}C-depleted front spreading northward, rather than a shoaling of deeper water, because the $\Delta^{14}C$ is lower at 2000 m than at 2500 m. This increase in the volume of I/D SSW at the expense of ^{14}C-rich NSW formation at the 15.4-ka event is the likely cause of the ^{14}C plateau in the atmosphere.

At the end of the 15.4-ka event, the water column has an ''inverted'' profile with radiocarbon-poor water overlying radiocarbon-rich water (Figs. 2B and 4A). This inverted profile is analogous to GEOSECS profiles farther south in the modern west Atlantic, although the gradients are much smaller in the modern ocean. Deglacial intermediate SSW masses have previously been observed in benthic $\delta^{13}C$ records at lower latitudes in the Tasman Sea and at the Chatham Rise (*45*, *46*), but this is the first time that water with such low $\Delta^{14}C$ is seen at I/D depths so far north.

Bolling-Allerod to Holocene. The Bolling begins at ~14.6 ka on the Greenland Ice Sheet Project 2 (GISP2) time scale (*2*, *47*) and is widely recorded across the Northern Hemisphere (Fig. 1). Cd/Ca ratios (*6*) and Nd isotopes (*48*), from the North and South Atlantic, respectively, show that NSW dominated the deep Atlantic during the Bolling. The modeled and observed $\Delta^{14}C$ records converge with one another at this time (Fig. 1, arrow d), suggesting that the Bolling ocean was capable of drawing down as much radiocarbon as the modern carbon cycle. Consistent with this suggestion, we observe that the $\Delta^{14}C$ depth profile is more like the modern ocean than at any time since the glacial (*49*) (Fig. 4B). The entire water column is filled by radiocarbon-rich water, with deep water (3500 m) only 70‰ lower than the atmosphere (Fig. 4B). Radiocarbon-rich water also invaded the eastern Atlantic at this time (*50*). The timing of this NSW flush is consistent with the reinvigoration of export from the North Atlantic as recorded by Pa/Th (*44*).

The end of the Bolling is characterized by cooling (Fig. 1) (*2*) and is coincident with a 700-year, 160‰ drop in deep-ocean $\Delta^{14}C$ at 3500m (Fig. 2C) (*51*).The resulting Allerod water-column $\Delta^{14}C$ profile is consistent with Cd/Ca ratios, which indicate that the deep Atlantic was filled by a mix of NSW and SSW (*6*). This mixture was ~170‰ offset from the atmosphere, as shown by BF-PF pairs from 3500 m (13.9 ka) and 4250 m (13.6 ka) and an equatorial deep-sea coral from 2300 m (~14.0 ka) (*23*, *24*). This reduction in the amount of deep NSW formation is the likely cause of the divergence of modeled and atmospheric $\Delta^{14}C$ records in the transition from the Bolling to the Allerod (Fig. 1).

The beginning of the Younger Dryas, at 12.9 ka, is characterized by a large decrease in Northern Hemisphere temperature (Fig. 1). The $\Delta^{14}C$ depth profile is ''inverted'' between 1700 m and 2500 m (Fig. 4B) (*20*, *28*), but at ~2500 m there is a sharp transition back to radiocarbon-depleted deep water, ~300‰ offset from the atmosphere (Fig. 4B) (*19*). The increased proportion of radiocarbon-depleted SSW at I/D and abyssal depths is the likely cause of the marked divergence between the modeled and observed atmospheric $\Delta^{14}C$ records (Fig. 1, arrow e) (*34*, *52*). During the Younger Dryas, at ~12 ka, Eltgroth *et al.* (*28*) report a $\Delta^{14}C$ ''spike'' at I/D water depths from corals on either side of the North Atlantic [New England Seamount (Fig. 2C, arrow z) and Azores]. This transient flushing of well-ventilated NSW is synchronous with a kink in the atmospheric $\Delta^{14}C$ record and a brief warm event observed in both Antarctica and Greenland ice cores (Fig. 1, arrow z).

At the end of the Younger Dryas, four BF-PF pairs spanning 1400 m to 4250 m all have the same ~100‰ $\Delta^{14}C$ offset from the atmosphere (Fig. 3A). This final flush of radiocarbon-rich NSW fills the entire depth range of the western Atlantic by 10.6 ka, drawing down ^{14}C and causing the modeled and observed atmospheric $\Delta^{14}C$ to converge. This overall circulation pattern and associated carbon cycle is similar to the modern day (Fig. 1, arrow f).

Conclusions. The deep-ocean radiocarbon pattern supports the notion of the bipolar seesaw: When the deep ocean was flushed by radiocarbon-rich NSW, Greenland was warming, and when NSW was replaced by SSW, Greenland was cooling. The I/D ocean is much more variable, with multiple switches between radiocarbon-depleted and radiocarbon-enriched water masses (Fig. 3). These I/D-ocean radiocarbon events are associated with small climate changes observed in both Greenland and Antarctic ice cores. Increasing $\Delta^{14}C$ in the I/D ocean is associated either with no temperature change or with warming. Decreasing I/D ocean $\Delta^{14}C$ is associated with interruptions in the rise of temperature out of the LGM. This pattern is inconsistent with a bipolar seesaw link between cross-equatorial heat flux and climate change. I/D water-mass variability does not have as large an effect on climate as deep-ocean variability but may play an important role in modulating the atmospheric carbon reservoir.

References and Notes

1. R. B. Alley *et al.*, *Nature* **362**, 527 (1993).
2. T. Blunier, E. J. Brook, *Science* **291**, 109 (2001).
3. W. S. Broecker, *Paleoceanography* **13**, 119 (1998).
4. W. B. Curry, D. W. Oppo, *Paleoceanography* **20**, PA1017 (2005); 10.1029/2004PA001021.
5. D. W. Oppo, S. J. Lehman, *Science* **259**, 1148 (1993).
6. E. A. Boyle, L. D. Keigwin, *Nature* **330**, 35 (1987).
7. T. M. Marchitto Jr., W. B. Curry, D. W. Oppo, *Nature* **393**, 557 (1998).
8. *D. dianthus* and *D. cristagalli* are two names for the same coral; the former is more widely used.
9. $^{14}C/^{12}C$ ratios are reported as $\Delta^{14}C$, the ratio of a sample to the preindustrial prenuclear atmospheric standard in units of ‰.
10. W. S. Broecker, S. Blanton, M. Smethie Jr., H. G. Ostlund, *Global Geochemical Cycles* **5**, 87 (1991).
11. M. Stuiver, P. D. Quay, H. G. Ostlund, *Science* **219**, 849 (1983).
12. W. S. Broecker, T. H. Peng, *Tracers in the Sea* (Lamont-Doherty Geol. Obs., Palisades, NY, USA, 1982).
13. M. Stuiver, H. G. Ostlund, *Radiocarbon* **22**, 1 (1980).
14. C. Wunsch, *Quat. Sci. Rev.* **22**, 371 (2003).
15. W. Broecker *et al.*, *Radiocarbon* **30**, 261 (1988).
16. W. S. Broecker *et al.*, *Radiocarbon* **32**, 119 (1990).
17. J. C. Duplessy *et al.*, *Radiocarbon* **31**, 493 (1989).
18. N. J. Shackleton *et al.*, *Nature* **335**, 708 (1988).
19. L. D. Keigwin, *Paleoceanography* **19**, PA4012 (2004); 10.1029/2004PA001029.
20. J. F. Adkins, H. Cheng, E. A. Boyle, E. R. M. Druffel, R. L. Edwards, *Science* **280**, 725 (1998).
21. S. J. Goldstein, D. W. Lea, S. Chakraborty, M. Kashgarian, M. T. Murrell, *Earth Planet. Sci. Lett.* **193**, 167 (2001).
22. N. Frank *et al.*, *Earth Planet. Sci. Lett.* **219**, 297 (2004).
23. A. Mangini *et al.*, *Nature* **392**, 347 (1998).
24. A. Schroder-Ritzrau, A. Mangini, M. Lomitschka, *Earth Planet. Sci. Lett.* **216**, 399 (2003).
25. J. F. Adkins, G. M. Henderson, S. L. Wang, S. O'Shea, F. Mokadem, *Earth Planet. Sci. Lett.* **227**, 481 (2004).
26. All corals in this study were collected in May 2003 using the deep submergence vehicle Alvin, ensuring that the depth of each coral (between 1100 and 2500 m) was well known; the corals were collected at, or near, life position. The Seamount locations are Muir, 33°30′N, 62°30′W; Manning, ~38°0′N, 60°30′W; and Gregg 39°0′N, 61°0′W.
27. Materials and methods are available as supporting material on *Science* Online.
28. S. Eltgroth, J. F. Adkins, L. F. Robinson, J. Southon, M. Kashgarian, *Paleoceanography*, in preparation.
29. L. D. Keigwin, M. A. Schlegel, *Geochem. Geophys. Geosyst.* **3**, AN1034 (2002).
30. L. D. Keigwin, J. P. Sachs, Y. Rosenthal, E. A. Boyle, *Paleoceanography* **20**, 10.1029/2004PA001074 (2005).
31. L. D. Keigwin, G. A. Jones, *J. Geophys. Res. Oceans* **99**, 12397 (1994).
32. L. D. Keigwin, G. A. Jones, S. J. Lehman, E. A. Boyle, *J. Geophys. Res. Oceans* **96**, 16811 (1991).
33. K. A. Hughen *et al.*, *Radiocarbon* **46**, 1059 (2005).
34. K. A. Hughen *et al.*, *Science* **303**, 202 (2004).
35. J. W. Beck *et al.*, *Science* **292**, 2453 (2001).
36. R. Muscheler *et al.*, *Earth Planet. Sci. Lett.* **219**, 325 (2004).
37. After its initial production, ^{10}Be is attached to aerosols and removed from the atmosphere with a 1- to 2-year residence time. Because this process is completely different from the ^{14}C removal mechanism, variations in the ratio of wet and dry deposition at Greenland could lead to ^{10}Be accumulation rate changes that are not correlated with cosmogenic radionuclide production rate changes. We do not consider this possible source of error in our analysis.
38. G. M. Raisbeck *et al.*, *Geophys. Res. Lett.* **8**, 1015 (1981).
39. P. J. Reimer *et al.*, *Radiocarbon* **46**, 1029 (2005).

40. R. Gersonde *et al.*, *Paleoceanography* **18**, 1061 (2003); 10.1029/2002PA000809.
41. R. Gersonde, X. Crosta, A. Abelmann, L. Armand, *Quat. Sci. Rev.* **24**, 869 (2005).
42. R. Gersonde, U. Zielinski, *Palaeogeogr. Palaeoclimatol. Palaeoecol.* **162**, 263 (2000).
43. S. R. Hemming, *Rev. Geophys.* **42**, RG1005 (2004); 10.1029/2003RG000128.
44. J. F. McManus, R. Francois, J. M. Gherardi, L. D. Keigwin, S. Brown-Leger, *Nature* **428**, 834 (2004).
45. H. C. Bostock, B. N. Opdyke, M. K. Gagan, L. K. Fifield, *Paleoceanography* **19**, PA4013 (2004).
46. K. Pahnke, R. Zahn, *Science* **307**, 1741 (2005).
47. P. M. Grootes, M. Stuiver, J. W. C. White, S. Johnsen, J. Jouzel, *Nature* **366**, 552 (1993).
48. A. M. Piotrowski, S. L. Goldstein, S. R. Hemming, R. G. Fairbanks, *Earth Planet. Sci. Lett.* **225**, 205 (2004).
49. Two samples at 15.0 ka (1180 m) and 14.3 ka (1221 m), both from Gregg Seamount, have $\Delta^{14}C$ values ~25‰ and ~0‰ below the atmosphere, respectively. From the end of Heinrich 1 to ~14.2 ka, the atmospheric radiocarbon content dropped at least as fast as the decay rate, leading to a situation in which the decrease in the radiocarbon content of the atmosphere could "overtake" the decay rate in an isolated water mass. Two samples from the end of the Younger Dryas are also within error of the atmospheric value and lie at the end of a marked drop in the atmospheric radiocarbon content (28).
50. L. C. Skinner, N. J. Shackleton, *Paleoceanography* **19**, PA2005 (2004); 10.1029/2003PA000983.
51. This trend is well constrained by five BF-PF pairs, three of which (including the oldest and youngest) are from the same core.
52. K. A. Hughen *et al.*, *Nature* **391**, 65 (1998).
53. R. G. Fairbanks *et al.*, *Quat. Sci. Rev.* **24**, 1781 (2005).
54. Y. J. Wang *et al.*, *Science* **294**, 2345 (2001).
55. We acknowledge the Comer Foundation for Abrupt Climate Change, the Henry Luce Foundation, the American Chemical Society Petroleum Research Fund, and NSF grant numbers OCE-0096373 and OCE-0095331. We also thank all members of the cruise AT7-35 to the New England Seamounts.

Supporting Online Material
www.sciencemag.org/cgi/content/full/1114832/DC1
Materials and Methods
Tables S1 to S3
References and Notes

13 May 2005; accepted 24 October 2005
Published online 3 November 2005;
10.1126/science.1114832
Include this information when citing this paper.

REPORTS

Postseismic Mantle Relaxation in the Central Nevada Seismic Belt

Noel Gourmelen* and Falk Amelung

Holocene acceleration of deformation and postseismic relaxation are two hypotheses to explain the present-day deformation in the Central Nevada Seismic Belt (CNSB). Discriminating between these two mechanisms is critical for understanding the dynamics and seismic potential of the Basin and Range province. Interferometric synthetic aperture radar detected a broad area of uplift (2 to 3 millimeters per year) that can be explained by postseismic mantle relaxation after a sequence of large crustal earthquakes from 1915 to 1954. The results lead to a broad agreement between geologic and geodetic strain indicators and support a model of a rigid Basin and Range between the CNSB and the Wasatch fault.

Some of the largest earthquakes in North America during the 20th century were located in the Central Nevada Seismic Belt (CNSB), one of the known actively deforming areas in the Basin and Range (Fig. 1). The 1915 Pleasant Valley earthquake [seismic magnitude (M_s) 7.2 to 7.6], the 1932 Cedar Mountain earthquake (M_s 7.2), and the 1954 Rainbow Mountain–Fairview Peak–Dixie Valley earthquake sequence (four events, M_s 6.8 to 7.2, in a 6-month period) were right lateral to normal slip events, and ruptured a noncontinuous stretch of north-northeast striking range front faults ~250 km in length.

The present-day deformation across the CNSB is puzzling for two reasons: (i) The deformation rate during Holocene time is believed to be 0.5 to 1.3 mm/year (*1*–*4*), which is lower than the 2 to 4 mm/year measured by Global Positioning System (GPS) data (*5*–*7*); and (ii) GPS measurements reveal a zone of east-west contraction east of the CNSB (*5*–*9*) that is difficult to reconcile with current geodynamic models of the region, which involve east-west extension and right-lateral shear. One possible explanation for these two discrepancies is that the GPS data record not only the long-term deformation, but also transient deformation associated with viscous or viscoelastic relaxation of the lower crust or upper mantle after the last century's earthquakes (*7*, *8*, *10*). We used 8 years of interferometric synthetic aperture radar (InSAR) data to investigate ongoing deformation in the CNSB.

The SAR imagery covers a swath nearly 700 km long (seven conventional SAR frames) acquired by the European Remote Sensing Satellites ERS-1 and ERS-2 between 1992 and 2000 to investigate crustal deformation at the CNSB (*11*). InSAR measures changes in the radar line-of-sight (LOS) distance between the satellite and the surface of Earth; it is most sensitive to vertical movement and somewhat sensitive to east-west movements (*12*). A ground velocity map in LOS direction is shown in Fig. 1. The map was obtained by averaging (stacking) eight independent long-term interferograms, each spanning 4 to 7 years (Table 1). Most of the interferograms have perpendicular baselines smaller than 100 m. We used these pairs because larger baselines lead to decorrelation of the interferometric phase. We obtained the velocity map by dividing the cumulative LOS displacement of the interferograms by the cumulative interferogram period of 37 years. We assumed that uncertainties associated with the satellite orbits cause linear phase ramps across the interferogram and removed any linear trend from the data.

The resulting ground velocity map shows a bulge with LOS velocity as high as ~3 mm/year of relative motion with respect to the margin of the interferograms, centered in the epicentral area of the 1915 Pleasant Valley and 1954 Dixie Valley earthquakes. About 1 to 2 mm/year is detected in the areas of the Fairview Peak and Cedar Mountain earthquakes. The map also shows an area of subsidence in the northern part of the interferogram in the area of the Lone Tree gold mine, presumably caused by groundwater pumping in support of open-pit mining operations.

To test whether the observed phase signature is real deformation or a processing artifact, we generated another stack using eight interferograms covering shorter time periods (each <4 months, total time span ~2 years). Because no deformation is expected from such a stack, a residual signal would reveal processing, atmospheric, or orbital artifacts. To obtain comparable LOS velocities, we divided the cumulative LOS displacement of the short-term stack by the cumulative time of the long-term stack (37 years). The averaged LOS velocities based on the long-term stack (Fig. 2) show a long-wavelength signal of ~3 mm/year of LOS velocity, but the short-term stack does not show this signal. This result indicates that the

Division of Marine Geology and Geophysics, Rosenstiel School of Marine and Atmospheric Sciences, University of Miami, Miami, FL 33149, USA.

*To whom correspondence should be addressed. E-mail: ngourmelen@rsmas.miami.edu